RAPID COMMUNICATION

Optical coherence tomography using broad-bandwidth XUV and soft X-ray radiation

**S. Fuchs · A. Blinne · C. Rödel · U. Zastrau · V. Hilbert ·
M. Wünsche · J. Bierbach · E. Frumker · E. Förster ·
G.G. Paulus**

Abstract We present a novel approach to extend optical coherence tomography (OCT) to the extreme ultraviolet (XUV) and soft X-ray (SXR) spectral range. With a simple setup based on Fourier-domain OCT and adapted for the application of XUV and SXR broadband radiation, cross-sectional images of semiconductors and organic samples becomes feasible with current synchrotron or laser-plasma sources. For this purpose, broadband XUV radiation is focused onto the sample surface, and the reflected spectrum is recorded by an XUV spectrometer. The proposed method has the particular advantage that the axial spatial resolution only depends on the spectral bandwidth. As a consequence, the theoretical resolution limit of XUV coherence tomography (XCT) is in the order of nanometers, e.g., 3 nm for wavelengths in the water window (280–530 eV). We proved the concept of XCT by calculating the reflectivity of one-dimensional silicon and boron carbide samples containing buried layers and found the expected properties with respect to resolution and penetration depth confirmed.

S. Fuchs (✉) · A. Blinne · C. Rödel · U. Zastrau · V. Hilbert ·
M. Wünsche · J. Bierbach · E. Förster · G.G. Paulus
Institute of Optics and Quantum Electronics, Friedrich-Schiller
University of Jena, Max-Wien-Platz 1, 07743 Jena, Germany
e-mail: silvio.fuchs@uni-jena.de

S. Fuchs · C. Rödel · E. Förster · G.G. Paulus
Helmholtz Institute Jena, Helmholtzweg 4, 07743 Jena, Germany

E. Frumker
Joint Laboratory for Attosecond Science, National Research
Council of Canada and University of Ottawa, 100 Sussex Drive,
Ottawa, ON K1A 0R6, Canada

1 Introduction

Optical coherence tomography is a well-established method to retrieve three-dimensional, cross-sectional images of biological samples in a non-invasive way using near-infrared radiation [1]. In fact, OCT has become a state-of-the art approach for a number of significant applications in ophthalmology [2] and microscopy [3]. The technique exploits the low temporal coherence of broadband radiation causing a rapid decay of interference structures in a Michelson-type interferometer. In traditional or time-domain OCT, the sample reflectivity is scanned in axial directions while the depth of the layer to be imaged can be varied by changing the reference arm length. The axial resolution of OCT is in the order of the coherence length l_c which depends on the central wavelength λ_0 and the spectral width (FWHM) $\Delta\lambda_{\mathrm{FWHM}}$ of a light source with a, e.g., Gaussian shaped spectrum

$$l_c = \frac{2\ln 2}{\pi} \frac{\lambda_0^2}{\Delta\lambda_{\mathrm{FWHM}}}. \tag{1}$$

As a consequence, the axial resolution only depends on the spectral rather than geometrical properties of the radiation. This is particularly interesting for applications where a high numerical aperture is not feasible. OCT with broadband visible and near-infrared sources typically reach axial (depth) resolutions in the order of a few micrometers [1–3].

Within the last decade and in conjunction with the quickly developing sector of advanced material design, the scale length of interest has dropped from micrometers to a few nanometers. Both the semiconductor circuit industry, aiming at fast and power-saving solutions, as well as structural biology and environmental chemistry with their enormous interest in nanostructures, call for resolutions in the nanometer regime. The ideas presented here take advan-

tage of the fact that the coherence length can be significantly reduced if broadband XUV and SXR radiation is used.

Microscopy using XUV and SXR radiation has regularly ineluctable practical restrictions imposed by the optics and sources available in this regime. Coherence tomography with short wavelengths can circumvent some of these limitations in principle. A major limitation of XUV radiation is the absorption within a few tens or hundreds of nanometers [4] depending on the actual composition of the material and the wavelength range. Consequently, XUV coherence tomography (XCT) can only display its full capabilities when used in the transmission windows of the sample materials. For instance, the silicon transmission window (30–99 eV) corresponds to a coherence length of about 12 nm assuming a rectangular spectrum and an absorption length of about 200 nm, thus suggesting applications for semiconductor inspection. In the water window at 280–530 eV as defined by the K absorption edges of carbon and oxygen, respectively, a coherence length as short as 3 nm can be achieved and highlights possible applications of XCT for life sciences.

2 Theory of XUV coherence tomography

The theory of short-wavelength coherence tomography (XCT) can be most easily discussed on the basis of a Michelson-type interferometer, which is also the prototype of OCT setups. The result of the following analysis will show that XCT is possible in principle. For a proof-of-principle calculation, a non-absorbent sample structured as a stack of discrete reflecting layers is considered; see Fig. 1. With the wave number in the media $k = 2\pi/\lambda$ and the temporal domain frequency ω a spectral component of the electric field of the light source can be written as

$$E_{\text{source}}(k, z, t) = \mathcal{E}(k)e^{i(kz-\omega t)}. \tag{2}$$

Assuming a time-integrating detector at the output of an interferometer setup with an ideal achromatic beamsplitter with equal splitting ratio, the detector signal is given by the temporally averaged sum of all partial field components

$$\mathcal{I}_D(k, z_R) = \frac{1}{2}\left\langle \left| \frac{\mathcal{E}(k)}{\sqrt{2}}\sqrt{R_R}e^{i(2kz_R-\omega t)} \right.\right.$$
$$\left.\left. + \sum_{n=1}^{N}\frac{\mathcal{E}(k)}{\sqrt{2}}\sqrt{R_{Sn}}e^{i(2kz_{Sn}-\omega t)} \right|^2 \right\rangle, \tag{3}$$

where z_R is a delay adjusted by moving the reference arm, R_R the wavelength-independent intensity reflectivity of the reference mirror, and R_{Sn} and z_{Sn} the wavelength-independent intensity reflectivity and depth of the nth layer of the sample structured discretely for purposes of proof-of principle [5].

An expansion of this equation results in a spectral interferogram, which contains the complete information on the depths and the reflectivities of the sample layers:

$$\mathcal{I}_D(k, z_R) = \frac{\mathcal{S}(k)}{4}(R_R + R_{S1} + R_{S2} + \cdots)$$
$$+ \frac{\mathcal{S}(k)}{2}\sum_{n=1}^{N}\sqrt{R_R R_{Sn}}\cos\left[2k(z_R - z_{Sn})\right]$$
$$+ \frac{\mathcal{S}(k)}{4}\sum_{n\neq m=1}^{N}\sqrt{R_{Sn}R_{Sm}}\cos\left[2k(z_{Sn} - z_{Sm})\right]. \tag{4}$$

Here, $\mathcal{S}(k) = |\mathcal{E}(k)|^2$ is the intensity spectrum of the light source. In a time-domain OCT device, the detector is not wavelength sensitive and integrates over all spectral components of the electric field. Assuming a Gaussian spectrum $\mathcal{S}(k) = \frac{\mathcal{S}_0}{\Delta k\sqrt{\pi}}e^{-[\frac{k-k_0}{\Delta k}]^2}$ (central wave number k_0 and width Δk), this integration leads to the detector signal, which depends only on the reference arm length.

$$\mathcal{I}_D(z_R) = \frac{\mathcal{S}_0}{4}(R_R + R_{S1} + R_{S2} + \cdots)$$
$$+ \frac{\mathcal{S}_0}{2}\sum_{n=1}^{N}\sqrt{R_R R_{Sn}}\underbrace{e^{-(z_R-z_{Sn})^2\Delta k^2}}_{\Gamma(z_R-z_{Sn})}$$
$$\times \cos\left[2k_0(z_R - z_{Sn})\right]$$
$$+ \frac{\mathcal{S}_0}{4}\sum_{n\neq m=1}^{N}\sqrt{R_{Sn}R_{Sm}}e^{-(z_{Sn}-z_{Sm})^2\Delta k^2}$$
$$\times \cos\left[2k_0(z_{Sn} - z_{Sm})\right]. \tag{5}$$

Equation (5) describes a typical time-domain OCT signal as shown in Fig. 1. Only the second term depends on z_R. The other terms produce a constant offset $\mathcal{I}_{\text{DC}}$. For an observation of a modulation of the detector signal a difference of the optical path length between the reference arm and the sample arm smaller than the coherence length l_c is required; see (1). The measured detector signal as a function of the delay gives the reflectivity distribution of the sample broadened by the coherence function Γ that is linked to the spectral intensity $\mathcal{S}(k)$ via the Wiener–Chinchin theorem.

$$\Gamma(\zeta) = \text{FT}^{-1}\left[\mathcal{S}(k)\right]. \tag{6}$$

Thus, the coherence function is directly connected to the axial resolution. Another well-known OCT setup is the so-called Fourier-Domain OCT. Here, for a fixed reference arm length, the entire spectral dependence of the spectral interferogram (4) is measured with a spectrometer at the detector position. This procedure has the particular advantage that
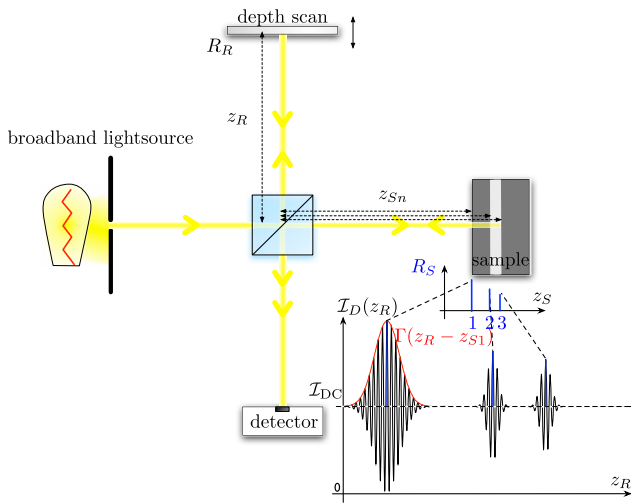
Fig. 1 Schematic of a typical OCT setup: In a Michelson interferometer, the reference path beam and the sample path beam interfere at the detector. The detected signal depends on the wavelength and the reference arm length. In traditional time-domain OCT, the detector integrates over all wavelengths. The depth structure of the sample can be obtained by scanning the length of the reference arm. The $\mathcal{I}_D(z_R)$-graph was computed using (5) and reveals the sample structure. The width of the coherence length l_c must be smaller than the distance of the layers to each other to resolve the layer positions

Fig. 2 Proposed setup of a common-path Fourier-domain OCT setup in the XUV spectral range: The XUV beam is reflected at the layer surfaces of the sample. The beams interfere and cause a modulated reflected spectrum that can be measured with a grating spectrometer. The toroidal mirror images the sample surface onto the CCD camera

the entire information is obtained with a single measurement rather than performing mechanical depth scans necessary in time-domain OCT. The information about the sample structure can be extracted from a Fourier transform. Using (6), it can be seen that a Fourier transform of the spectral interferogram (4) that depends on $k = 2\pi n(\omega)/\lambda_{\text{vacuum}}$, has an intensity distribution depending on the depth only.

$$
\begin{aligned}
I_D(z, z_R) = {} & \frac{\Gamma(z)}{4}(R_R + R_{S1} + R_{S2} + \cdots) \\
& + \sum_{n=1}^{N} \frac{\sqrt{R_R R_{Sn}}}{4} \\
& \times \underbrace{\int_{-\infty}^{\infty} \Gamma(\zeta)\delta\big(z \pm 2(z_R - z_{Sn}) - \zeta\big)\,\mathrm{d}\zeta}_{\Gamma[z+2(z_R-z_{Sn})]+\Gamma[z-2(z_R-z_{Sn})]} \\
& + \sum_{n \neq m=1}^{N} \frac{\sqrt{R_{Sn} R_{Sm}}}{8} \\
& \times \underbrace{\int_{-\infty}^{\infty} \Gamma(\zeta)\delta\big(z \pm 2(z_{Sn} - z_{Sm}) - \zeta\big)\,\mathrm{d}\zeta}_{\Gamma[z+2(z_{Sn}-z_{Sm})]+\Gamma[z-2(z_{Sn}-z_{Sm})]}\,. \quad (7)
\end{aligned}
$$

In fact, this expression contains the entire information about the sample reflectivity and thus its structure. The discrete δ-structure is convoluted with the coherence function $\Gamma(z)$ that limits the resolution in a similar way as in time-domain OCT. The first line of (7) contains the DC-components of the
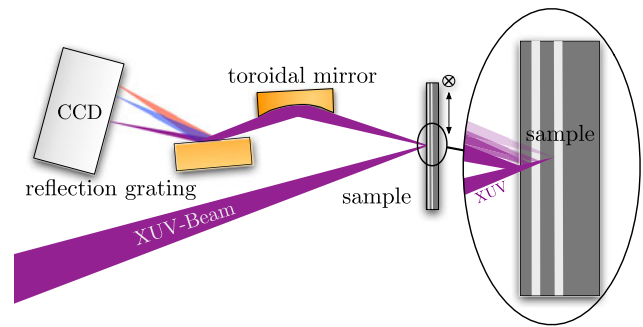
signal, the second line cross-correlation terms, and the third line's terms are called autocorrelation terms. The cross and autocorrelation terms each contain the information about the sample's structure.

In most cases of Michelson-type OCT, the reflectivity of the reference mirror is much higher than the reflectivities of the sample layers. Therefore, the amplitudes of the autocorrelation terms are weak as compared to the cross-correlation terms. Hence, the autocorrelation terms are usually not evaluated and only the cross-correlation components are used to reconstruct the depth structure.

The realization of a classical Michelson interferometer in the XUV regime is highly demanding. The wavelength is about two orders of magnitude shorter as compared to visible and infrared radiation. This would call for extraordinary precision with respect to the flatness of optical surfaces, including the beam splitter, and finally also with regard to the mechanical stability of the components [6]. In order to overcome these problems, we propose to use a variant of Fourier-domain OCT setup called common-path Fourier-domain OCT [7]. The reference wave and the sample wave share the same path; see Fig. 2. Strikingly, using this variety of OCT, a beam splitter can be completely avoided [8]. However, the cross-correlation terms do not exist in this simplified OCT scheme. Accordingly, the spectral interferogram (4) is reduced to a DC-component and the autocorrelation terms; see (8).

$$
\begin{aligned}
\mathcal{I}_D(k) = {} & S(k)(R_{S1} + R_{S2} + \cdots) \\
& + S(k) \sum_{n \neq m=1}^{N} \sqrt{R_{Sn} R_{Sm}} \cos\big[2k(z_{Sn} - z_{Sm})\big]. \quad (8)
\end{aligned}
$$

A well-defined depth structure cannot be extracted due to ghost peaks in the Fourier transform of (8) from the interaction between the layers; see (9).
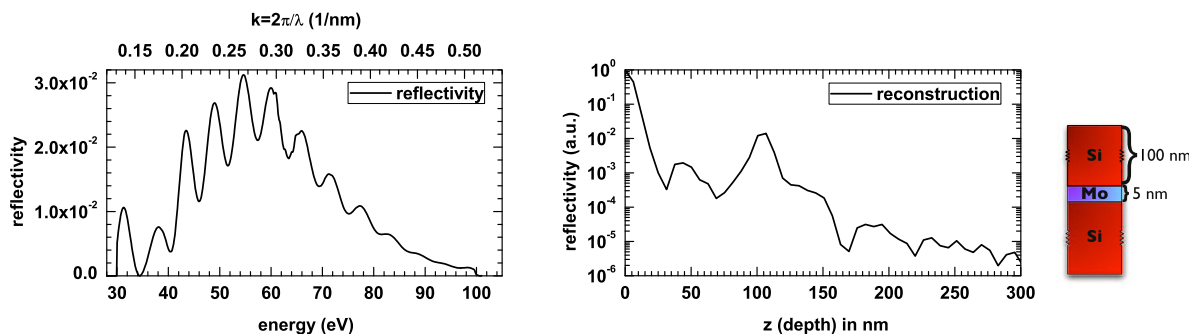
Fig. 3 (*left*) Simulated reflected XUV spectrum of a Si substrate in vacuum with a 5-nm Mo layer buried under a 100-nm Si layer in the silicon transmission window at an incidence angle of 75° to the surface, s-polarized. (*right*) Fourier transform of the calculated reflected spectrum and sketch of the sample structure. The width of the peak at 100 nm is 13 nm (FWHM). The Mo layer clearly can be detected. However, its thickness cannot be resolved because the coherence length of the radiation is too large

$$I_D(z) = \Gamma(z)(R_{S1} + R_{S2} + \cdots)$$

$$+ \sum_{n \neq m = 1}^{N} \frac{\sqrt{R_{Sn} R_{Sm}}}{2}$$

$$\times \underbrace{\int_{-\infty}^{\infty} \Gamma(\zeta) \delta\big(z \pm 2(z_{Sn} - z_{Sm}) - \zeta\big) \, d\zeta}_{\Gamma[z + 2(z_{Sn} - z_{Sm})] + \Gamma[z - 2(z_{Sn} - z_{Sm})]}. \qquad (9)$$

For an absorbing sample, however, the reflected signal of the top layer surface is commonly larger than the attenuated reflections from deeper layers. The components of the autocorrelation term, which contain the top layer reflection, can outbalance the remaining components comprising only inner layer reflections. In this context, the top layer reflection takes the place of a reference beam. In order to increase this effect, a thin, strongly reflecting top layer (e.g., 5 nm Au) should be added to the sample. As already mentioned, merely a Fourier transform of the reflected spectrum needs to be computed for retrieving the structural information.

Unfortunately, the wave number $k = n\omega/c$ cannot be calculated without uncertainties, due to the unknown refractive index $n(\omega, z_S)$ of the sample. In the simplest case, one could approximate the sample as an ideal non-dispersive object and calculate the Fourier transform. However, accuracy and precision will decrease, if the media is dispersive. Therefore, the absolute values of the depths of the buried layers as computed by the Fourier frequencies have an uncertainty due to the inaccurate assumptions about the refractive index and the optical path lengths in the sample, respectively. In order to reduce these inaccuracies, we assume a dispersion given by the material that is dominant in the sample. In practice, the dominant substance is known for most nano-scale samples of interest. For the present case of XCT, knowledge of the dominant substance is a prerequisite for determining the transparency window anyhow.

3 Simulated reflected signals of a layer structure based on a matrix method algorithm

In order to test the ideas outlined above, a simulation of the reflectivity of a multilayer structure is essential. For this purpose, we developed a computational model based on the matrix method algorithm [9] and using the refractive index database from [4]. Molybdenum (Mo) and Lanthanum (La) layers buried under a silicon layer were investigated as a sample for proof-of-principle studies in the silicon transmission window. These materials have a well-pronounced absorption contrast with respect to the silicon substrate. Further, layer combinations of different materials, e.g., B_4C and SiO_2 were investigated for the water window. The simulations of the sample reflectivity in both spectral ranges show strong modulations in the reflected spectrum, as predicted by the theory of coherence tomography.

In the example, shown in Fig. 3, a Mo layer is buried under 100 nm of silicon which has an absorption length of 200 nm in the spectral window used. The resolution of the Fourier transformed signal is in the order of the corresponding coherence length of 12 nm. Hence, a layer buried under 100 nm of silicon is expected to produce well-separated reflections. On the other hand, the individual reflections at the front and the rear Mo surfaces cannot be resolved. If the Mo layer thickness is increased to 100 nm, the reflection from the rear Mo surface can still not be resolved due to the small absorption length in Molybdenum; see Fig. 4.

The Fourier transformed signal, especially in the silicon window, shows a few strong artifacts due to the rectangle-like boundaries of the spectral window; see the upper panels of Fig. 5. For improving the contrast between real reflectivity and Fourier artifacts, filter functions can be applied. The respective results using the Kaiser–Bessel filter are shown in the lower panels of Fig. 5. This kind of filtering tends to reduce the resolution of the reflection peaks—the more the stronger the attenuation caused by
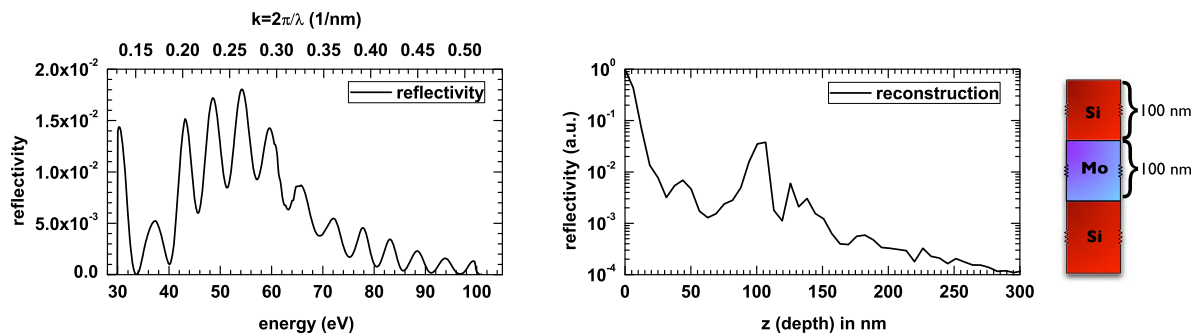
Fig. 4 The same analysis as in Fig. 3. Here, we assume a 100-nm Mo layer. Its thickness can still not be resolved, in this situation, however, due to the strong absorption of Mo. The width of the peak in the right panel at 100 nm is 12.3 nm (FWHM)
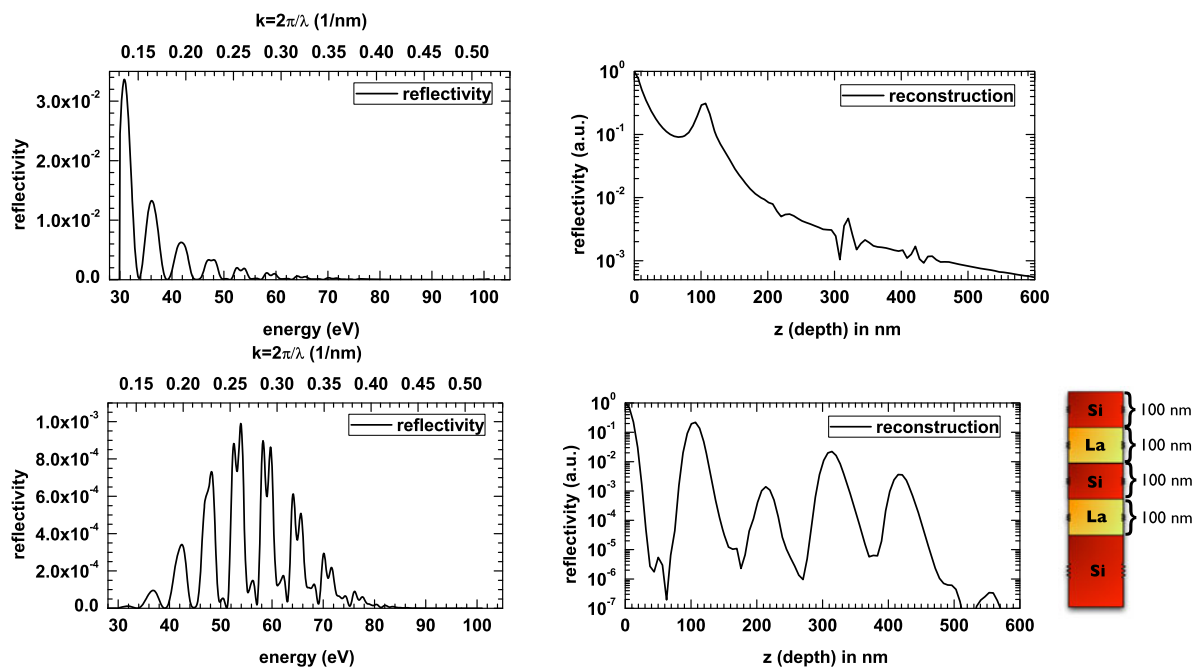

Fig. 5 (*left*) Simulated reflected XUV spectrum of a Si substrate in vacuum with two 100-nm La layers buried and separated with 100-nm Si layers in the silicon transmission window at an incidence angle of 75° to the surface, s-polarized. A rectangular filter function

(*upper panels*) or a Kaiser–Bessel filter function (*lower panels*) are used. (*right*) Fourier transform of the calculated reflected spectrum and sketch of the sample structure. The rectangular filter function results in artifacts while the smoother filter function slightly decreases resolution

the applied filter. In our example, the suppression of the Fourier artifacts due to the filter overcompensates this effect.

For the water transmission window, we investigate a 1-nm Lanthanum layer buried under a 100-nm B_4C layer. As expected, the resolution is on the order of 3 nm; see Fig. 6. The reflectivity in the SXR range is much smaller as compared to the XUV regime used for the silicon window. In order to measure such a signal in a tolerable time, a source with a sufficient photon flux is required.

Let us perform a rough estimation to show that such an experiment is indeed possible: The simulations show a reflectivity of the used materials of about 10^{-2} in the XUV range and about 10^{-5} in the SXR range. The ef-

ficiency of a typical XUV spectrometer consisting of a toroidal mirror and a gold transmission grating [10] or a reflection grating [11] depends strongly on the photon energy and is on the order of 10^{-2} at 50 eV. A typical XUV CCD camera needs about 10^4–10^5 photons for saturation. With a synchrotron undulator source, photon fluxes of about 10^{12} photons/s at 0.1% bandwidth are possible. This means that exposure times of a few microseconds in the XUV regime and some seconds in the SXR are required, proving the feasibility of the scheme. A proof-of-principle experiment was performed at synchrotron radiation sources at DESY (Deutsches Elektronen-Synchrotron) and BESSY (Berliner Elektronenspeicherring-Gesellschaft für Synchrotronstrahlung), which produce the required pho-
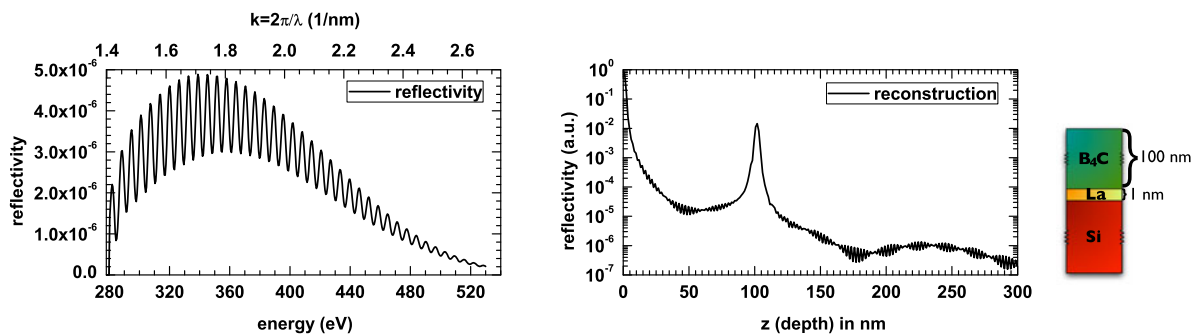
Fig. 6 (*left*) Simulated reflected XUV spectrum of a Si-substrate in vacuum with a 1-nm La layer buried under a 100-nm B₄C layer in the water transmission window at an incidence angle of 75° to the surface, s-polarized. (*right*) Fourier transform of the calculated reflected spec-

trum and sketch of the sample structure showing that the theoretical limits can be also achieved in the water transmission window. The width of the peak at 100 nm is 3.4 nm (FWHM)
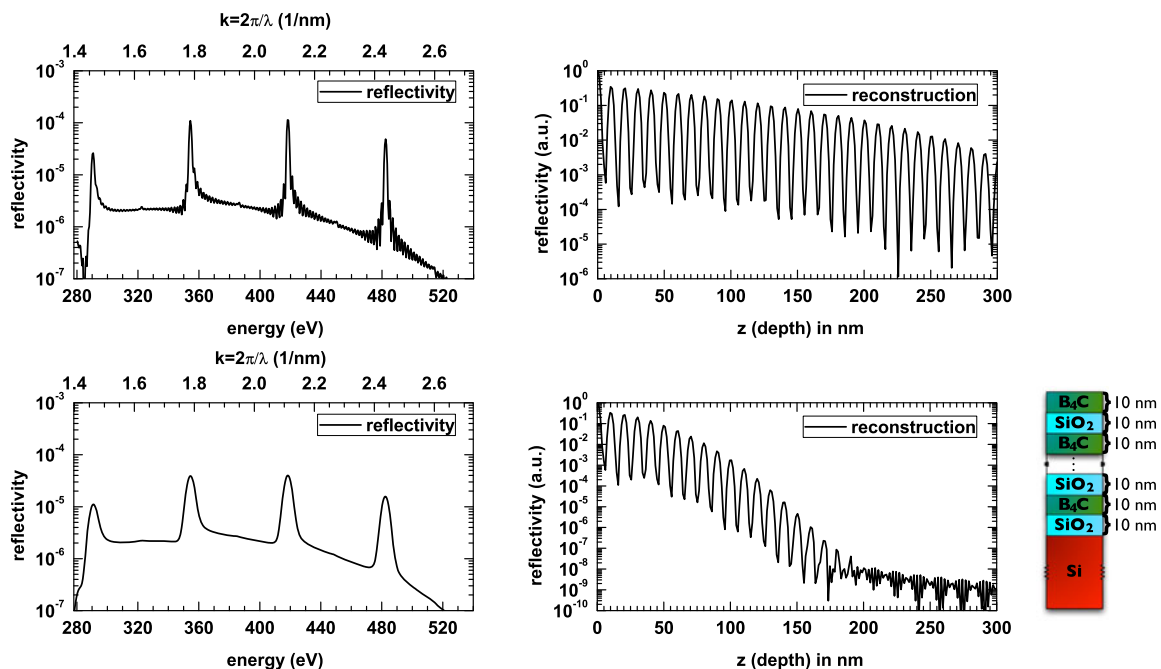

Fig. 7 Simulated reflected XUV spectrum of a Si substrate in vacuum with a stack of alternating B₄C and SiO₂ layers, each of 10 nm thickness in the water transmission window. The incidence angle is 75° to the surface, s-polarized. Results for an ideal spectrometer are displayed in the *upper left panel*, results for a spectrometer with a re-

alistic resolution (Gaussian spectrometer point spread function with a width of 5 eV FWHM) in the *left lower panel*. The *panels on the right* display the corresponding Fourier transform of the calculated reflected spectrum and a sketch of the sample structure

ton flux. The broad spectrum could be achieved by changing the undulator gap over time. The results will be published soon.

Furthermore, the broadband XUV radiation from laser plasmas could be a suitable source. Using a calibrated spectrometer, we observed photon fluxes at the entrance of the spectrometer of about 10^{11} photons per laser shot at 0.1% bandwidth [12] in experiments irradiating solid density targets with intensities of approximately 10^{19} W/cm^2. The corresponding spectrum is very broad and smooth and the source dimension is small, i.e., very suitable for XCT.

It is remarkable that the resolution of OCT is mainly independent of the spectral resolution of the spectrometer. In order to demonstrate this, the reflected spectrum of the sample is convoluted with a spectrometer point spread function which is assumed to be Gaussian; see Fig. 7. The limited spectral resolution only reduces the maximum detectable structure depth due to the fact that the modulation frequency of the spectrum is not longer resolvable. Consequently, the structural information of the 10 nm layers as shown in the lower panel of Fig. 7 is not affected by the reduction of spectral resolution. The high-frequency parts of the spec-

trum vanish and the maximum detectable depth decreases to 180 nm in this example.

4 Conclusion

We have presented calculations for a proof-of-principle experiment of optical coherence tomography using broad bandwidth XUV and SXR radiation (XCT). Evidence has been given that synchrotron and laser plasma XUV and soft X-ray sources offer sufficient flux for XCT. This strongly suggests its application as a new non-invasive tomographic method to investigate nanometer-scale structures of layered systems and simple three-dimensional samples by lateral raster scanning. We emphasize in particular the opportunities offered by the silicon and water spectral windows. The former is highly relevant for a new non-destructive method of imaging semiconductor devices. The water window, on the other hand, is known for its significance in the life sciences. The remarkable contrast of carbonic and oxygenic materials in the SXR range promises high-quality images of biological samples. The axial resolution of the imaged structures is only affected by the dynamic range of the spectrometer's detector and the width and wavelength of the used transmission.

References

1. D. Huang, E.A. Swanson, C.P. Lin, J.S. Schuman, W.G. Stinson, W. Chang, M.R. Hee, T. Flotte, K. Gregory, C.A. Puliafito, J.G. Fujimoto, Science **254**, 1178 (1991)
2. M.R. Hee, J.A. Izatt, E.A. Swanson, D. Huang, J.S. Schuman, C.P. Lin, C.A. Puliafito, J.G. Fujimoto, Arch. Ophthalmol. **113**, 325 (1995)
3. G.J. Tearney, M.E. Brezinski, B.E. Bouma, S.A. Boppart, C. Pitris, J.F. Southern, J.G. Fujimoto, Science **276**, 2037 (1997)
4. B.L. Henke, E.M. Gullikson, J.C. Davis, At. Data Nucl. Data Tables **54**, 181 (1993)
5. W. Drexler, J.G. Fujimoto, *Optical Coherence Tomography* (Springer, Berlin, 2008)
6. A.S. Morlens, P. Zeitoun, L. Vanbostal, P. Mercere, G. Faivre, S. Hubert, P. Troussel, C. Remond, R. Marmoret, F. Delmotte, M.F. Ravet, M. Rouillay, Laser Part. Beams **22**, 279 (2004)
7. A.B. Vakhtin, D.J. Kane, W.R. Wood, K.A. Peterson, Appl. Opt. **42**, 6953 (2003)
8. G.G. Paulus, C. Rodel, US Patent 20080212075
9. M. Born, E. Wolf, *Principles of Optics: Electromagnetic Theory of Propagation, Interference and Diffraction of Light* (Cambridge University Press, Cambridge, 1997)
10. J. Jasny, U. Teubner, W. Theobald, C. Wulker, J. Bergmann, F.P. Schäfer, Rev. Sci. Instrum. **65**, 1631 (1994)
11. R.R. Fäustlin, U. Zastrau, S. Toleikis, I. Uschmann, E. Förster, T. Tschentscher, J. Instrum. **5**, 2004 (2010)
12. C. Rodel, M. Heyer, M. Behmke, M. Kübel, O. Jäckel, W. Ziegler, D. Ehrt, M.C. Kaluza, G.G. Paulus, Appl. Phys. B **103**, 295 (2011)